ELSEVIER

Journal of Nuclear Materials 279 (2000) 31–45

journal of nuclear materials

www.elsevier.nl/locate/jnucmat

The precipitation behaviour of ITER-grade Cu–Cr–Zr alloy after simulating the thermal cycle of hot isostatic pressing

Uwe Holzwarth *, Hermann Stamm

European Commission, Joint Research Centre, Institute for Health and Consumer Protection, Via E. Fermi 1 (T.P.202), I-21020 Ispra (VA), Italy

Received 20 September 1999; accepted 8 December 1999

Abstract

The precipitation behaviour of Cu–0.75Cr–0.105Zr (wt%) alloy for fusion reactor applications has been investigated after thermal treatments similar to those expected during joining procedures by hot isostatic pressing. A bimodal distribution of coarse precipitates with spacings larger 1 μm and tiny precipitates with spacings between 30 and 40 nm was observed by scanning electron microscopy (SEM) and transmission electron microscopy (TEM), respectively. The coarse precipitates resist solution annealing treatments and do not contribute to mechanical strength. Two types of microscopically small precipitates were observed, which exhibit strain field contrast in TEM and are responsible for the mechanical strength of the aged alloy. A fine dispersion of these precipitates with a mean size of 2.3 nm and a density of 3.3×10^{22} m^{-3} is related with maximum strength. Hardening is most compatible with an Orowan mechanism. These precipitates are only obtainable when the joining procedure is terminated with a minimum cooling rate of about 1 K/s.

PACS: 28.52.Fa; 61.72.Ff; 81.05.Bx; 81.40.Cd

1. Introduction

Cu–Cr–Zr alloys with chromium and zirconium contents of 0.6–0.8 and 0.07–0.15 wt%, respectively, are considered as potential heat sink material for the ITER divertor vertical target since they exhibit high strength and high thermal conductivity [1,2]. The main problem to be solved is related to the thermal stability of this alloy during divertor manufacture especially when joining procedures require the application of temperatures which may cause solution annealing or overaging of the alloy. This motivated recent studies on the possibilities to recover the mechanical and physical properties of the ITER-grade Cu–Cr–Zr alloy after hot isostatic pressing [3,4]. In [3] hot isostatic pressing has been simulated by a solution annealing at 970°C for 20 min. Whereas solution annealing is normally terminated by quenching in water, quenching cannot be applied to finish hot isostatic pressing. In this case the component will cool in air or in an inert atmosphere and the cooling rate will be much smaller. Therefore, the present authors investigated the effect of cooling rate after hot isostatic pressing on the efficacy of subsequent heat treatments to recover the desired mechanical properties of the precipitation hardened alloy [3]. This investigation showed that such a recovery is only achievable if the solution annealing, i.e., the hot isostatic pressing is terminated with a cooling rate of at least 1–2 K s^{-1} [3]. It has been concluded that lower cooling rates lead to long holding times in the temperature range of aging and to an overaging of the material. In this case the insufficient tensile properties cannot be improved by any of the tested aging treatments to be applied thereafter [3]. Also the results of Singh et al. [4] underline the strong sensitivity of the mechanical properties to details of the heat treatment and to possible mechanical pre-treatments.

* Corresponding author. Tel.: +39-0332 785 194; fax: +39-0332 785 388.

E-mail address: uwe.holzwarth@jrc.it (U. Holzwarth).

0022-3115/00/$ - see front matter
PII: S0022-3115(99)00285-8

The present electron microscopic investigation was motivated in order to check the conclusions drawn in [3] on the basis of the observed changes of tensile strength and thermal diffusivity of the alloy and in order to quantify the precipitate densities after certain heat treatment sequences. Furthermore, an assessment of the microstructural changes during the long cooling phase after the joining procedure and during the subsequent heat treatments is expected to be helpful for proposing possible improvements in the joining procedure, the composition or the pre-treatment of the alloy.

In literature there is no clear picture on the precipitation behaviour and the microstructure properties of Cu–Cr–Zr. The largest amount of information is available on the binary Cu–Cr alloys which are of interest because of their excellent age-hardening properties. The small amount of literature covers a rather broad range of different compositions, different production processes and mechanical pre-treatments often coming to different conclusions. There is general agreement that the high strength of the properly aged alloy is brought about by tiny chromium-rich precipitates with typical dimensions around 10 nm or even smaller [5–8]. This seems to hold also for the ternary Cu–Cr–Zr alloy [4,9,10]. The nature of these chromium-rich particles is, however, not yet clearly understood. In their TEM studies Knights and Wilkes [8] found homogeneously distributed needle-shaped particles of 5–10 nm size in various stages of aging. From the absence of non-matrix reflections in the electron diffraction patterns they concluded that these particles were coherent and of face-centered cubic (fcc) structure [8]. After reviewing literature Chakrabarti and Laughlin [11] concluded that this may indeed be possible. Rdzawski and Stobrawa [12] succeeded in a chemical isolation of the chromium precipitates in a Cu–0.94Cr (wt%) alloy and investigated the isolated precipitates by X-ray phase analysis. The surprising result was that even the isolated coherent precipitates preserved a metastable fcc structure [12]. Komen and Rezek [7] observed in their Cu–0.35Cr (wt%) alloy a mixture of coherent particles showing strain field contrast and rod shaped particles which appeared non-coherent. These authors attributed the additional reflexes in their electron diffraction pattern to chromium-rich non-coherent particles with body-centered cubic (bcc) structure. Similar results were reported from further TEM investigations, which found precipitation accompanied by non-matrix reflections which could be ascribed to bcc chromium precipitates [5,6,10]. However, there are different opinions on the orientation relations between these precipitates and matrix. Whereas Weatherly et al. [6] found that the Kordjumov–Sachs relations are obeyed, Tang et al. [10] found agreement with those of Nishyama–Wassermann. Moreover, from strain field observations accompanied by modelling Weatherly et al. [6] came to the conclusion that the chromium bcc phase can be coherently accommodated by the fcc copper matrix. In this case extremely large shear stresses of up to 1/5 of the shear modulus should be present in and around the particles although no evidence for dislocation nucleation could be found related to the particles [6].

Although the strengthening in the ternary Cu–Cr–Zr alloy seems to be due to the same type of chromium precipitates, the situation appears to be complicated by the additional alloying with zirconium. It will be shown that in this case a pronounced coarse precipitation occurs additionally to the precipitation of tiny particles. Such a feature has not been reported for the binary Cu–Cr alloy. This problem is associated with the lack of generally accepted phase relationships in the Cu–Cr–Zr system. Recent theoretical [13] and experimental [14] investigations by Zheng et al. indicate that three phases Cr, Cu_5Zr and Cu should exist in this system but no Cr_2Zr as postulated in many earlier investigations.

2. Experiments

2.1. Material and specimen preparation

The Cu–Cr–Zr alloy had an alloying content of 0.75 wt% Cr, 0.105 wt% Zr and a total impurity content below 0.01 wt%. The material was received in the cold rolled and solution annealed state with a grain size of (40 ± 10) μm [3]. Grain growth was observed after the heat treatments F and G (definition see below), which resulted in a grain size around 90 μm [3].

Six classes of TEM specimens were prepared. The labels (A), (B), (F), (G), (K) and (L) correspond to the heat treatment sequences defined in [3] and compiled below. All treatments were performed in an argon atmosphere in a quartz tube. Furnace cooling was realized by switching off the furnace; out-of-furnace cooling by pulling the quartz tube out of the furnace. In these cases mean cooling rates of 0.05 K and 1 K s^{-1} were achieved, respectively. For details on the cooling curves and the relevant cooling rates the reader is referred to [3]. The heat treatment sequences relevant for the present considerations are:

(A) Solution annealing at 970°C for 20 min followed by water quenching. The material has been received in this state.

(B) After treatment (A) the material was subjected to an aging treatment at 475°C for 3 h followed by furnace cooling.

(F) The solution annealing at 970°C for 20 min was repeated and terminated by furnace cooling.

(G) After treatment (F) the material was subjected to an aging reatment at 475°C for 3 h followed by furnace cooling.

(K) The solution annealing at 970°C for 20 min was repeated and terminated by out-of-furnace cooling.

(L) After treatment (K) the material was subjected to an aging treatment at 475°C for 3 h followed by furnace cooling.

These heat treatment sequences were performed on small Cu–Cr–Zr cylinders of 2 mm height and 3.5 mm in diameter. In order to minimize mechanical loading during the preparation of the TEM specimens the size of the cylinders was reduced to a thickness of about 0.3 mm and a diameter of 2.5 mm by immersion in nitric acid (65%). Then a gentle grinding was applied using 4000 SiC paper to smoothen the surface roughened by the etching in nitric acid before electrolytical jet-polishing. In this preparation step the thickness of the small plates was reduced to 0.25 mm. Jet-polishing was performed at −45°C using a mixture of 500 ml nitric acid and 1000 ml ethanol as electrolyte. A voltage of 32 V was applied. During jet-polishing a current of 650–700 mA was measured. Perforation was obtained after about 2 min.

The quality of the produced TEM specimens was checked by optical microscopy. The specimen surfaces exhibited a structure which indicated the presence of coarse precipitates with spacings of several μm. This structure appeared to be less pronounced for specimens in the conditions A and B. In the conditions F and G the density of these precipitates was higher and they were distributed in striations along the direction of cold rolling. Their distribution in the small electron-transparent area around the perforation indicated that these coarse precipitates could hardly be investigated by TEM. Hence, a second imaging technique was required to get a complete overview on the precipitation behaviour of this alloy.

2.2. Electron microscopy

The transmission electron microscopy (TEM) was performed with a Jeol 4000 FX instrument at the Max-Planck-Institut für Metallforschung, Stuttgart, Germany. The instrument was equipped with a specimen holder which allowed a specimen tilt of ±10° with respect to the incident electron beam. Due to the rather large grain size only two or three grains could be examined in the visual field around the perforation and the choice of the diffraction conditions was therefore limited. For TEM imaging it was attempted to realize dynamic two beam conditions, which could approximately be achieved for [0 2 2], [1 1 1] and [1 1 3]-type diffraction vectors. Most micrographs were taken in bright field (BF) conditions. Dark field (DF) diffraction conditions and especially weak beam conditions were difficult to control due to the limited specimen tilt.

For a quantitative evaluation of precipitate densities the thickness of the TEM foils was estimated by counting thickness fringes. Typical values range between 230 and 380 nm.

The coarse, large precipitates on the electrolytically polished surfaces of the TEM specimens were lateron examined in a LEO 435 VP scanning electron microscope (SEM). These precipitates were also analyzed by energy dispersive X-ray analysis (EDX) in the SEM. The spot size for this analysis was 1 μm and thus in many cases larger than the particles to be analyzed.

3. Results

3.1. Transmission electron microscopy

The results of the TEM are compiled in Fig. 1, which shows the typical features in the conditions B, F, G, K and L, which will be described in detail below. The micrographs taken in condition F are somehow untypical since they show the rare cases of observable precipitates. No micrograph is shown in the solution annealed condition A since, as expected, no precipitates could be observed in this case.

3.1.1. Observed precipitation contrast

Small misfitting precipitates with strain field contrast give rise to contrast features described in literature as lobe–lobe contrast. The contrast behaviour has been explained first by Ashby and Brown [15] and later modified by McIntyre and Brown [16] taking into account that the classical Ashby–Brown rules might not be obeyed by very small particles. McIntyre and Brown introduced a parameter P_S which helps to predict the contrast behaviour to be expected under two-beam conditions. This parameter is defined as $P_S = g|\varepsilon|r_0^3\xi_g^{-2}$, where ε is the misfit strain and r_0 the constrained particle radius. $g = d_{hkl}^{-1}$ denotes the modulus of the active diffraction vector and ξ_g the corresponding extinction length. An estimate of the maximum possible value of P_S assuming a typical particle size of 5 nm [5,9] and a misfit strain of 0.1, yields values between 0.003 and 0.005 for all reasonable diffraction conditions (g_{hkl} and ξ_g taken from [17]). The maximum reported misfit strain in Cu-based alloys reported in [35] is 0.0428. Hence, 0.1 is a conservative assumption. Since this value is below McIntyre and Brown's critical value of $P_S \leqslant 0.2$ we expect to observe the precipitates as small black/white lobes with a line of no contrast perpendicular to the active diffraction vector, when particles lie close to the surfaces of the foil, and as black dots in the center of the foil, both in bright and dark field images.

A closer look on the micrographs B (BF), B (DF) and L (BF) in Fig. 1, where precipitates are clearly visible, reveals that these features are only obeyed by a part of the precipitates. Two groups of precipitates have to be distinguished. A first group which shows lobe–lobe contrast or black dots. However, a clear line of contrast is often difficult to identify and its orientation deviates in

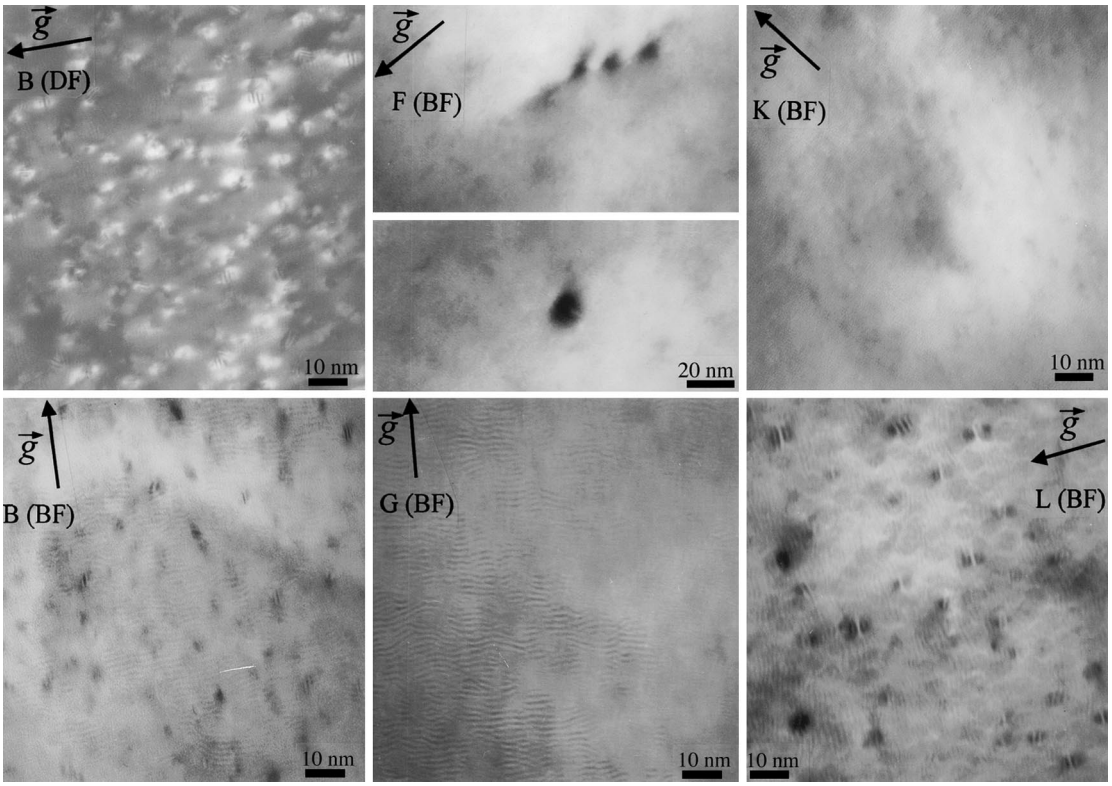

Fig. 1. Synopsis of the TEM results. Presented are two micrographs in condition B, taken under bright field (BF) and dark field (DF) conditions which show a homogeneous distribution of precipitates (i) showing lobe–lobe contrast or being imaged as black dots and (ii) fringed precipitates. In conditions F and G precipitates are visible only occasionally. In condition K, very few small fringed precipitates are observable. The subsequent aging treatment leads to homogeneously distributed precipitates in condition L. The diffraction vectors are of $\langle 1\,1\,1\rangle$-type for B (DF and BF), F and G, of $\langle 1\,1\,3\rangle$-type for K and of $\langle 0\,0\,2\rangle$-type for L.

many cases from being perpendicular to the active diffraction vector. In some cases this may however be caused by diffracting conditions deviating from the desired two-beam conditions. Most of the precipitates do not change their shape under different diffraction conditions, i.e., under different inclinations of the foil with respect to the incident electron beam. Thus one concludes that they are spherical. A second group of precipitates exhibits fringes predominantly parallel to the active diffraction vector with a spacing of about 1.25 nm.

Further features are spot-like or extended regions, which exhibit Moiré patterns. The smallest single areas covered by Moiré patterns had dimensions between 5 and 20 nm. In condition G only Moiré patterns could be observed. The Moiré fringes are predominantly perpendicular to the active diffraction vector (so-called parallel Moiré pattern) and have a mean spacing D between 1.25 and 1.45 nm under $\langle 1\,1\,1\rangle$ diffraction conditions. Moiré patterns form if a beam diffracted by two crystals with almost exactly equal or multiple lattice parameters is allowed to recombine with the transmitted beam to form the final image. In the simplest case an incoherent or semi-coherent platelet can be formed in or on the TEM foil having the same orientation of the lattice planes than the surrounding matrix. In the present case $D = a_m a_p/(a_m - a_p)$ holds [17,18], and one obtains $a_p \approx 0.18$ nm for the second involved lattice parameter. This value is most compatible with diffraction from (2 1 1)-type lattice planes of simple cubic Cu_2O which might be formed on the surface of the TEM specimens. Additional chemical information, e.g., delivered by EELS or an EDAX nanoprobe, would be required to confirm these features. However, the phenomenon is well-known for TEM on copper and the fact that a rather large lattice misfit is not related with any strain field strongly supports the interpretation of these Moiré structures as surface oxidation phenomenon.

3.1.2. Precipitate densities and precipitate size

When determining the density and size distribution of precipitates, no distinction was made between the two types of precipitates showing lobe–lobe and fringed strain field contrast. The size of the precipitates which exhibit lobe–lobe contrast was determined along the line

Table 1
Quantitative evaluation of the TEM micrographs in the conditions B and L. The table compiles the arithmetic mean value of the precipitate size d (for Eq. (3), $2R = d$ holds), the number of evaluated precipitates N, their density ϱ_p and their mean three-dimensional interparticle spacing λ_p

Material state after heat treatment sequence	d (nm)	N	ϱ_p (m^{-3})	λ_p (nm)
B	2.3	1285	3.3×10^{22}	31
L	2.4	525	1.7×10^{22}	39

of no contrast. From those which were imaged as black dots the diameter of the dots was measured. The fringed particles are often larger along the fringes than perpendicular to them. Thus, their size was defined as their average length along the fringes and perpendicular to them. The obtainable data on particle sizes and densities are compiled in Table 1 and the size distributions of the precipitates are presented in Fig. 2. The smallest precipitates which could be identified exhibited a dot-like contrast with a diameter of about 0.5 nm. Due to the uncertainty to determine the size especially of the precipitates which exhibit lobe–lobe contrast it has been decided to group the precipitates in size classes. The smallest class, denoted 1 nm in Fig. 2 ranges from 0.5 to 1.4 nm, the 2 nm class ranges from 1.5 to 2.4 nm and so forth.

As expected, no precipitates could be detected in the solution-annealed and water-quenched condition A. After the aging treatment, i.e., in condition B, both groups of precipitates are homogeneously distributed. In condition B the arithmetic mean value of the precipitate size is 2.3 nm. The precipitate density was determined as 3.3×10^{22} m^{-3}, which is equivalent to a mean three-dimensional particle spacing of 31 nm. The microstructure of the specimens in condition B is considered as reference for a successful aging after solution-annealing since in this condition the alloy exhibits the maximum observed tensile strength and hardness [3].

In condition F, after solution annealing followed by slow furnace cooling some rather large, inhomogeneously distributed precipitates were observed. Their size ranges between 5 and 15 nm. Also after the aging treatment, in condition G, only a few large precipitates with a diameter between 10 and 20 nm were found. The density of these precipitates in conditions F and G is too low to be quantitatively determined. Smaller precipitates were not found under any of the applied diffraction conditions.

In condition K, i.e., after solution annealing followed by out-of-furnace cooling a few larger precipitates with diameters between 10 and 15 nm were observed. Also some tiny fringed precipitates could be identified with a size of about 1 nm. Their density was however too low to be quantified. The matrix exhibits some small and weak spot-like contrasts which easily faded away when tilting the specimen. The contrast features of our known precipitates could never be established on these spots. Hence these weak contrasts could not unambiguously be identified as precipitates. It might be that precipitates are responsible for such contrast features which are too small to be clearly visible by structure factor contrast.

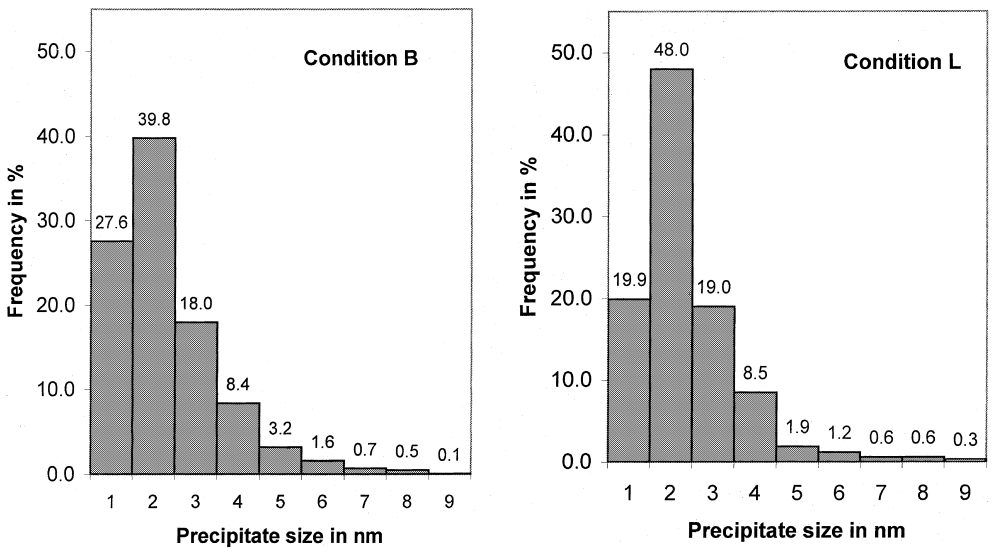

Fig. 2. Frequency of precipitate size as derived from TEM micrographs in the reference condition B and in the condition L. In these conditions 1285 and 525 precipitates were measured, respectively. For further details see Section 3.1.2.

Their size should then be well below 1 nm (cf. Section 4.1). After aging, in condition L, a homogeneous distribution of both types of precipitates was observed. In Fig. 2 the size distribution of the precipitates determined in this state is compared with the one obtained in condition B. The arithmetic mean value of the particle size was 2.4 nm and thus slightly increased. The size distributions show little difference apart of the reduced fraction of very small precipitates (1 nm group). The precipitate density of 1.7×10^{22} m^{-3} is, however, significantly lower than in the reference state. This density corresponds to a mean three-dimensional particle spacing of 39 nm.

3.2. Scanning electron microscopy

Fig. 3 gives a synopsis of the findings of SEM performed on the TEM specimens in the electrolytically

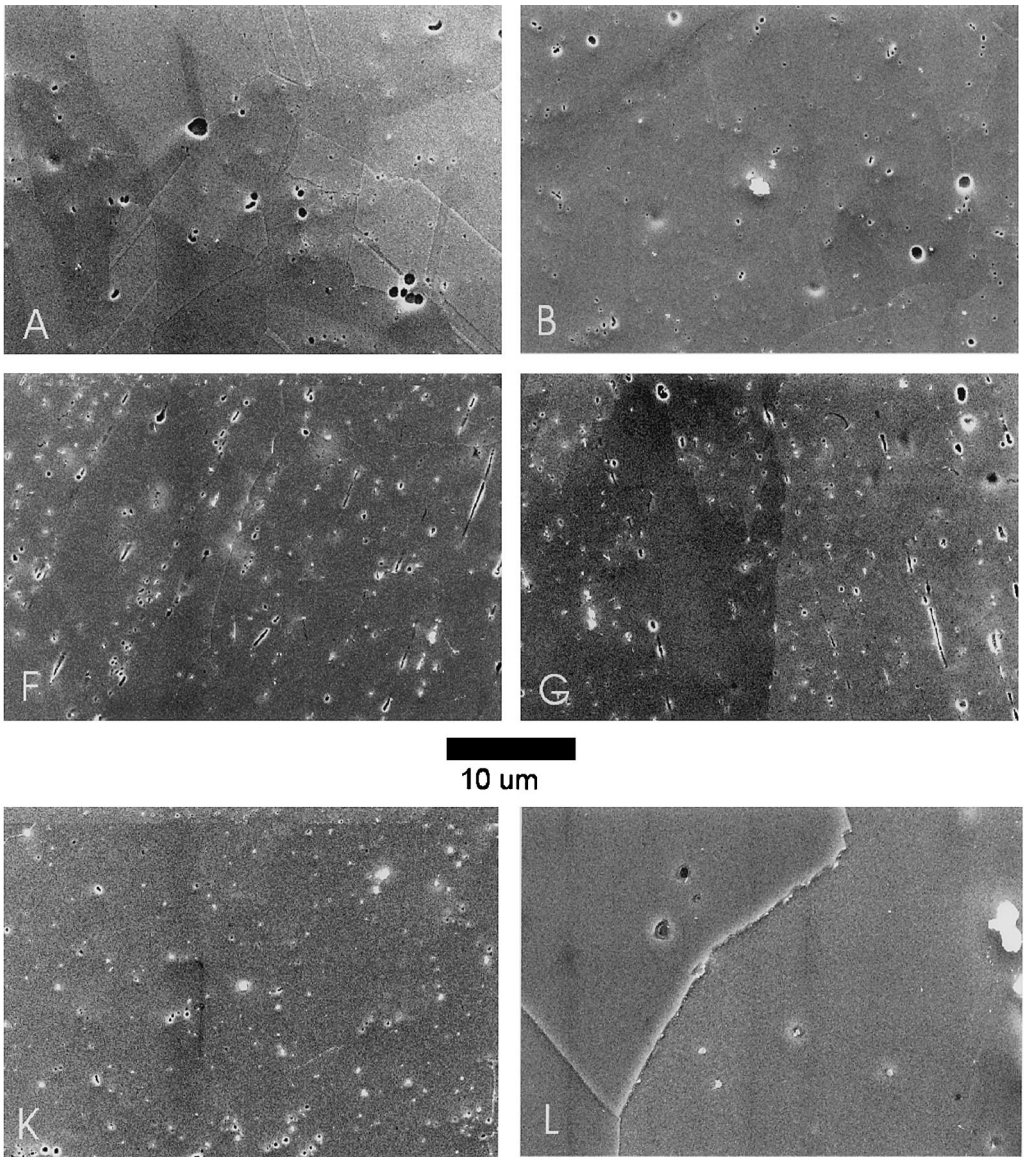

Fig. 3. Compilation of the SEM observations. Imaging was performed with secondary electrons. The left-hand side presents the solution annealed conditions (A, F, K). The right-hand side shows the corresponding conditions after aging (B, G, L). The composition of the white particles, the pits and the matrix was analyzed by EDX with a spatial resolution of 1 μm. The results are compiled in Table 2.

thinned region in a distance of typically 50–200 μm from the border of the perforation. Imaging was performed with secondary electrons. On the left-hand side the micrographs of the solution annealed specimens are shown. The solution annealing was always performed at 970°C for 20 min but it was terminated with different cooling rates achieved by quenching in water (condition A), furnace cooling (condition F) and out-of-furnace cooling (condition K). On the right-hand side the corresponding conditions after aging at 475°C for 3 h finished by furnace cooling are presented.

The common features of these micrographs are the presence of pits and white particles. The typical size of both ranges between 0.2 and 2 μm. In all cases both together cover a fraction of roughly 1% of the examined area. An EDX analysis revealed a Zr-enrichment in the white particles of up to about 20 at.%. The Zr concentration in the pits is below the detection limit which is about 1.4 at.% for this element. On the other hand, Cr contents between 29 and 100 at.% were determined. Since a lower Cr concentration is typical for smaller pits it may be attributed to the fact that the area analyzed by EDX (1 μm in diameter) contains also a contribution from the copper matrix. The observed composition ranges are given in Table 2. In cases like in Fig. 4 in which the pits were significantly larger than the EDX spot size of 1 μm, the bottom could be analyzed selectively. It was found that the presence of white contrast phenomena inside these pits was associated with the detection of Zr. Moreover, white particles are often visible at the boarder of the pits although their visibility is sometimes hampered by edge contrast. This observation might indicate that white particles and pits belong to the same precipitation phenomenon which might be described by the formation of a Zr-rich core which is surrounded by a chromium shell embedded in a copper matrix. We may tentatively assume that the pits are formed during jet-polishing, probably by preferential electrochemical attack of the interface between the zirconium-rich particle and its confining chromium shell. The coarse precipitates may then be washed out by the electrolyte jet leaving behind the pits.

From Fig. 3 differences in particle size and spatial distribution after the different thermal treatments become apparent. The solution annealed condition A typically exhibits a low density of comparably large pits of 1 to 2 μm in size. Although a precise quantitative assessment was not performed, the size of these pits appears to be slightly smaller after the aging treatment in state B and a further pronounced reduction in size is achieved in condition F and G. In these conditions the pits and the Zr-rich particles exhibit a maximum size of 1 μm. Some of the pits may however be elongated to a length of up to 10 μm. The elongation of the pits, their arrangement and the arrangement of the Zr-rich particles mark a preferential direction corresponding to the direction of cold rolling of the base material. After solution annealing followed by out-of-furnace cooling (condition K) pits and Zr-rich particles appear to be even smaller than 0.5 μm. The particles and pits are also aligned along a preferential direction, which is more obvious at lower magnification. The micrographs taken in condition L are the only ones indicating remarkable microstructural changes on a mesoscopic scale during the aging treatment. The comparison with

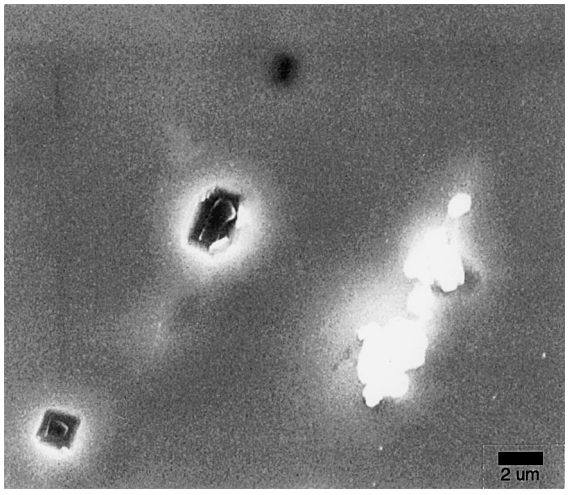

Fig. 4. Remnant white particles could often be observed at the boarder of the pits together with the less intense white edge contrast and in the depth of the pits.

Table 2
EDX analysis of white precipitates, pits and matrix (cf. Fig. 3). The conclusion on the most probable composition is based on the values for the largest precipitates and pits since an analysis of areas smaller than 1 μm is affected by the copper matrix

Analyzed sites	Measured composition (at.%)			Concluded composition
	Cu	Cr	Zr	
White particles	57–94	0–5	2–20	Cu_5Zr
Pits	0–71	29–100	0	Pure Cr
Matrix	94–100	0–6	0	Solid solution of Cr in pure Cu

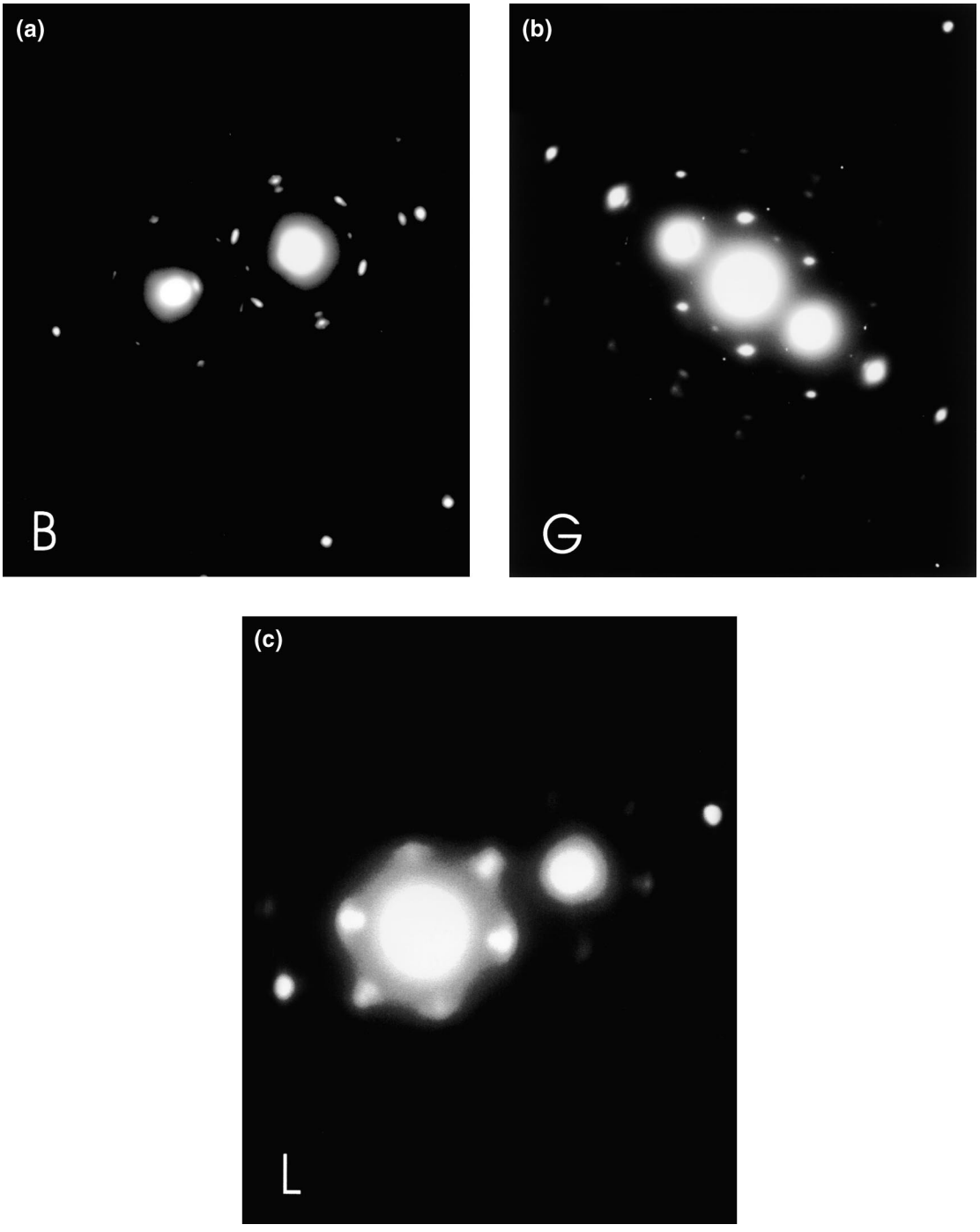

Fig. 5. (a) Typical diffraction pattern for condition B; zone axis close to [1 1 1], diffraction vector of type ⟨0 2 2⟩. (b) Typical diffraction pattern for condition G; zone axis close to [0 1 1], diffraction vector of type ⟨1 1 1⟩. (c) Typical diffraction pattern for conditions L; zone axis close to [0 1 1], diffraction vector of type ⟨1 1 3⟩.

the micrograph in condition K shows the precipitates have been grown to a size of up to 5 μm but their density is apparently reduced. In condition L small Zr-rich particles decorate grain boundaries; a phenomenon which has been much less prominent on the other specimens.

Table 3
Available crystallographic data on possible precipitated phases in the ternary Cu–Cr–Zr system as suggested in literature

Phase	Crystal structure	Lattice constants	Source
Cu–Cr solid solution	fcc ($Fm\bar{3}m$)	0 at.% Cr: $a = 0.36152$ nm 0.97 at.% Cr: $a = 0.36177$ nm 1.63 at.% Cr: $a = 0.36196$ nm	[20,21]
Cu_5Zr	fcc ($F\bar{4}3m$)	$a = 0.687$ nm	[24]
Cu_4Zr	Orthorhombic	$a = 0.504$ nm $b = 0.492$ nm $c = 0.664$ nm	[10]
Cu_3Zr		To be replaced by $Cu_{51}Zr_{14}$	[24,25]
$Cu_{51}Zr_{14}$	hcp (P6/m)	$a = 1.125$ nm $c = 0.8275$ nm	[25]
$CuZr_2$, $T \geqslant 1200$ K	Body-centered tetragonal (I4/mmm) Si_2Mo-type	$a = 0.32204$ nm	[22]
		$c = 1.11832$ nm Subcell: $a' = \sqrt{2}a$, $c' = 1/3c$	[23]
$CuZr_2$, $T \leqslant 1200$ K	Primitive tetragonal	$a = 1.592$ nm $c = 1.132$ nm	[24]
$CuZr_3$	Tetragonal (I4/mmm)	Same subcell as for $CuZr_2$ (?)	[23]
α-Cr_2Zr	Cubic ($Fd\bar{3}3m$) Cu_2Mg-type	$a = 0.7208$ nm	[26]
		Zr–Zr: 0.3121 nm; Cr–Cr: 0.2548 nm; Zr–Cr: 0.2988 nm	
β-Cr_2Zr	hcp ($P6_3/mmc$) $MgZn_2$-type	$a = 0.5102$ nm $c = 0.8532$ nm Zr–Zr: 0.3089 nm; Cr–Cr: 0.2551 nm; Zr–Cr: 0.2991 nm	[26]
Zr	hcp ($P6_3/mmc$)	$a = 0.3232$ nm $c = 0.5148$ nm	[27]
Cr	bcc (Im3m)	$a = 0.2885$ nm	[17]

4. Discussion

4.1. Interpretation of TEM results – the microscopic level

The present TEM investigation revealed that many of the precipitates which showed lobe–lobe contrast did not fully obey the classical Ashby–Brown rules for small misfitting spherical particles in a isotropic matrix [15]. The deviations are however not as severe as those reported by Tang et al. [10] who noted a random orientation of the line of no contrast with respect to the active diffraction vector. On the other hand, Singh et al. [4] did not mention deviations from the Ashby–Brown rules. Our estimate of the McIntyre–Brown parameter P_S showed, however, that the small size of the precipitates cannot account for such deviations. According to Degischer [19] deviations of the lines of no contrast from being perpendicular to the diffraction vector and contrasts other than lobe–lobe can occur due to the anisotropy of the copper matrix. This effect is especially pronounced for $\langle 1\,1\,1\rangle$-type diffraction conditions, which are unfortunately those which could be controlled best in regard of the limited specimen tilt.

Our findings agree well with those of Singh et al. [4] concerning the presence of several families of precipitates, namely, the coherent ones showing lobe–lobe contrast, and the fringed ones. In our quantitative analysis of precipitates we included both types of particles, showing strain-field contrast, due to their expected relevance for the mechanical properties. In our peak-aged condition B the mean size and density of these precipitates is smaller than those reported by Singh et al. [4] after solution annealing and subsequent aging with a mean size of 2.9 nm and a density of 5.9×10^{22} m^{-3}. These differences may however find their explanation in the different applied heat treatments. Singh et al. [4]

applied a lower annealing temperature (950°C) and a much shorter aging treatment (30 min). Since the data of these authors show that longer heat treatments reduce both particle size and density we may state reasonable quantitative agreement. The conditions of the alloy examined by Singh et al. [4] correspond to a condition less aged and another slightly more aged than our condition B.

The results of Correira et al. [9] are more difficult to compare with the present ones since these authors used a water atomized material consolidated by warm extrusion with much smaller grain size and different composition of Cu–2Cr–0.15Zr (at.%) and ≈ 0.2 at.% Si. From their TEM studies these authors reported the presence of precipitates showing strain field contrast with dimensions of about 4 nm in the peak-aged condition [9]. Other particles with a diameter of 10–15 nm exhibited Moiré fringes. An investigation with an EDAX nanoprobe indicated a significant concentration of zirconium in the fringed (Moiré-patterned) particles. It was concluded that these particles consist of Cu_5Zr and cause only a small hardening effect [9]. In their Cu–Cr alloy in slightly overaged condition they observed also particles with Moiré fringes of 12 nm in size and particles of 20–40 nm in diameter without coherency contrast. Correira et al. [9] concluded that in the binary Cu–Cr and the ternary Cu–Cr–Zr alloys strengthening is brought about by tiny coherent chromium particles which precipitate from a supersaturated copper matrix and loose coherency with proceeding overaging.

The main scope of the present TEM analysis was to obtain quantitative information on the precipitate densities responsible for the mechanical strength. Taking into account the difficulties when imaging the tiny precipitates and the exact determination of the foil thickness the values given for the precipitate densities are reliable within about 25%. There is still an uncertainty if all mechanically relevant precipitates are large enough to be visible at all, a doubt which has also been expressed by Correira et al. [9]. For a particle of thickness Δt, which is being imaged by structure factor contrast, the maximum relative intensity change is given by $\Delta I/I = 2\pi|1/\xi_g^p - 1/\xi_g^m|$ [18]. Here m and p denote matrix and particle, respectively. Assuming that the intensity change should not be less than 10% and with small extinction lengths [17,18] for low indexed diffracting planes of fcc copper and bcc chromium one calculates critical sizes in the nm range. Thus, the danger of missing particles relevant for mechanical strength may be real, especially when regarding the weak contrast features in condition K (cf. Section 3.1.2).

Fig. 5(a)–(c) show some typical diffraction patterns. Additional reflexes from whatever kind of precipitates and double reflexes are common features. Although other authors reported that they could successfully attribute additional reflexes to bcc chromium particles [7,9,10] or to other phases like Cu_4Zr [10] or to $CrCu_2Zr$ precipitates of the Heusler-type alloy [10] our diffraction patterns allowed no consistent correlation to any of the phases compiled in Table 3 in any reasonable orientation.

4.2. Coarse precipitation in Cu–Cr–Zr – the mesoscopic level

From the quantitative EDX analysis in SEM we may conclude that the phases formed in this alloy are pure copper, pure chromium and Cu_5Zr. This conclusion agrees well with recent theoretical [13] and experimental [14] examinations of the copper-rich corner of the ternary system Cu–Cr–Zr. The experimental investigations were however performed on alloys with much higher zirconium (>8 at.%) and chromium (>16 at.%) contents and lead to the conclusion that the chromium should be the primary phase embedded in a Cu_5Zr matrix [14]. From the Zr-rich white particles at the border of many pits and the presence of Zr detected in large Cr-rich pits we assume that white precipitates and pits are two aspects of the same feature. If the pits, in which pure chromium was detected, once surrounded the Zr-rich phase, which has electrolytically been polished away and whose composition corresponds best to Cu_5Zr, one might postulate that chromium precipitates around a core of Cu_5Zr embedded in a pure copper matrix.

The existence of coarse particles in Cu–Cr–Zr alloys which resist solution annealing was already observed in earlier investigations [4,28,29]. These particles are probably formed during the solidification of the alloy. This is to be expected for alloys with a composition close to or above the maximum solubility of 0.9 at.% (0.7 wt.%) in equilibrium and 1.8 at.% (1.45 wt%) after rapid quenching [11,20,30]. At the annealing temperature the solubility of chromium and zirconium in copper is about 0.4 wt% [29] and 0.15 wt.% [31], respectively. The existence of particles after solution annealing is therefore not surprising, but, their density and size are. From Fig. 3 we must conclude that nearly the complete alloying content is bound in coarse precipitates. Assuming that the microscopic particles observed in condition B are pure chromium, they can comprise not more than about 2% of the alloying content. The matrix has to be nearly depleted of chromium. Hence it seems strange that solution annealing does affect the coarse precipitates so little. With the exception of Rdzawski and Stobrawa [12] no similar problems with coarse precipitates were reported from binary Cu–Cr alloys with the composition Cu–0.4 at.%Cr [5] and Cu–0.35 wt%Cr [7]. These authors found coarse chromium precipitates of up to 1 μm in size after annealing and quenching from 1270 K in their Cu–0.94Cr (wt%) alloy. The chromium content of these alloys is below the solubility limit at annealing temperature. Since the same holds for the matrix of our

ternary alloy, one might expect that the coarse particles dissolve at least partially during annealing. The changes observable in Fig. 3 show that a modification of coarse precipitates indeed occurs concerning their size and distribution but with little effect on their volume fraction. Hypothetically we may explain this strange behaviour by the presence of zirconium. If we assume the white particles to consist of a Cu_5Zr core encapsulated by a chromium shell a rather stable binding of the chromium to this core might prevent the particles from complete dissolution during solution annealing. Depending on the stable thickness of the chromium shell only a fraction of the chromium may be free to re-enter the matrix. Spaic et al. [32] argued that the formation of coarse particles with an eutectic composition might explain their resistance against solution annealing.

4.3. The distribution of alloying atoms – a bimodal particle distribution

From the content of the alloying atoms Cr and Zr, one may expect to find precipitates with a volume fraction of at least 1%. From the size distribution of the precipitates visible in TEM (cf. Fig. 2) and their density one obtains volume fractions of 0.02% and 0.01% after the heat treatment sequences B and L, respectively. A similarly small volume fraction of microscopic precipitates was found by Long et al. [5]. These authors reported a volume fraction of 5×10^{-3} of rod shaped chromium precipitates with a diameter of about 35 nm and a length of around 60 nm in the peak aged condition of their Cu–0.4%Cr single crystals. Nothing is, however, reported on coarse precipitates, although the volume fraction of the chromium precipitates cannot account for a 0.4% chromium content.

The SEM investigation revealed that the alloying atoms are nearly completely concentrated in coarse precipitates with a size in the μm range and separations of up to 10 μm. From the particle spacings and confirmed by the measured mechanical properties of the alloy after the different heat treatments [3] we conclude that the coarse precipitates do not affect the mechanical properties of the alloy. This holds at least for the tensile properties, since the presence of coarse hard particles may reduce the fracture toughness of the alloy. Hence precipitation hardening is brought about by the tiny fraction of only 1% or 2% of the alloying atoms involved in the formation of the fine precipitates detectable by TEM with mean three-dimensional particle spacings between 30 and 40 nm.

Since coarse precipitates do not contribute to the mechanical properties, it should be the scope of material improvement to shift the alloying content from coarse to fine precipitation. The present findings show that solution annealing treatments are not suitable for this purpose since they cannot remove coarse precipitates. This corresponds to the findings by Apello and Fenici [29] who investigated solution heat treatments of the Cu–0.05Cr–0.15Zr (15 wt%) alloy Elbrodur HF. These authors concluded that their observed striations of coarse precipitates were already present before pre-deformation and solution annealing, and that only a few, if any, were dissolved during solution annealing treatments at 1000°C. Unfortunately, Apello and Fenici performed only a SEM study, thus they missed the microscopic precipitates in their material. A similar observation was also made by Morris et al. [33,34] on a Cu–2Cr–0.3Zr (at.%) alloy prepared by a spray deposition technique. After solution annealing at 980°C and aging at 600°C these authors found a bimodal distributions of fine precipitates with an average diameter of 15 nm and a mean spacing of 80 nm together with coarse particles of 0.85 μm in size and 2.8 μm interparticle distance [33].

A deeper understanding of the bimodal particle distribution is hampered by a still incomplete knowledge on the phase relations in the ternary Cu–Cr–Zr system. According to the solubility for chromium and zirconium in copper one would not expect such an amount of annealing resistant coarse precipitates. An interesting question concerns the coarse precipitates. Can they simply be regarded as excess content which might be removed, or is there an interaction between mesoscopic and microscopic precipitation if one varies the alloying content?

4.4. Precipitation hardening

For a consideration of precipitation hardening it is justified to neglect all coarse particles on a mesoscopic length scale because of their rather large spacings. For example, Long et al. [5] investigated a Cu–Cr–SiO_2 alloy and found that the strong silica particles contributed only 5% to the overall increase of the yield stress of the Cu–Cr alloy due to precipitation hardening. The main part is done by finely dispersed chromium particles, which illustrates that the average spacing of the obstacles along the dislocation line is of the utmost importance. The yield stress in the softest condition G must essentially be determined by the copper matrix probably plus a friction stress from the residual concentration of chromium and zirconium in solid solution. We can therefore assume that the volume fraction of hardening precipitates is $f \approx 0$ in condition G.

Models of precipitation hardening have been reviewed by several authors, e.g., by Ardell [35] and Gerold [36]. Usually the models give an expression for the increase of the critical resolved shear stress of a pure single crystal due to certain mechanisms of precipitation hardening. In order to compare the calculated values with experimental data on a polycrystalline material two problems have to be solved. Firstly, the polycrystalline yield stress data σ_0 have to be transformed into critical

Table 4
Comparison of the experimentally determined increase of the critical resolved shear stress $\Delta\tau_{crss}$ with the coherency strengthening and the Orowan model. For details see the second paragraph in Section 4.4. To assess ductility the uniform elongation ε_{UTS} and the elongation at fracture ε_{frac} are presented. All experimental values are mean values taken from [3]

Material condition (heat treatment sequence)	$\sigma_{0.2}$ (MPa)	ε_{UTS} (%)	ε_{frac} (%)	τ_{crss} (MPa)	$\Delta\tau_{crss}$ (MPa)		
						Calculation	
					Experim.	Orowan model	Coherency strengthening
A	110	39.5	51	36	22	(Solution hardening)	
B	272	16	25	89	75	58–146	5
G	42	48	57	14	0	0	0
L	160	27	38	52	38	40–100	3.5

resolved shear stress data τ_{crss}, which is done by dividing σ_0 by the Taylor factor $M = 3.06$. In our case we calculate $\tau_{crss} \approx \sigma_{0.2}/M$ from the proof stress data $\sigma_{0.2}$ at an offset of 0.2% plastic deformation as reported in [3], which are slightly higher than the yield stress σ_0. This effect is negligible compared to the uncertainty of the yield stress of the matrix which is required for a calculation of the yield stress increase caused by precipitation hardening. In the present case we assume that in condition G only residual solid solution atoms exert a friction stress on moving dislocations. On the other hand conditions B and L are hardened by strong tiny precipitates. This situation has been discussed by Lilholt [37] and Kocks [38] who concluded that as long as one of the two contributions to the critical resolved shear stress is due to weak obstacles and the other due to strong obstacles the former can be regarded as a friction stress and that these two contributions should be linearly additive. This allows us to estimate the precipitation hardening contribution to the critical resolved shear stress $\Delta\tau_{crss}$ by subtracting the value τ^{G}_{crss} in condition G from the other values τ^{i}_{crss} (i = B, L).

Fig. 1 indicates that strengthening in the conditions B and L is brought about by a random array of tiny coherent particles. The strengthening mechanism usually proposed in this case is that of dislocation pinning by the stress fields around the coherent precipitates [35,36]. A quantitative treatment of coherency strengthening yields for the increase of the critical resolved shear stress

$$\Delta\tau_0^{cs} = c_{cs}\,\varepsilon^{3/2} G \left(\frac{Rf}{b}\right)^{1/2}, \tag{1}$$

where ε denotes the misfit strain at the coherent interface, G the shear modulus of the matrix, b the modulus of the Burgers vector of matrix dislocations and R the radius of the particles and f their volume fraction. In literature the numerical constant c_{cs} ranges from 2.6 [35] to 3.7 [36]. The misfit strain can be estimated as shown by Eshelby [39] by

$$\varepsilon \approx \frac{2}{3}\frac{|a_p - a_m|}{a_m} \tag{2}$$

from the lattice parameters of the matrix, a_m, and the particle, a_p. If we tentatively assume that we have to deal with bcc chromium particles which precipitate with their $\{1\,1\,0\}$ planes on the $\{1\,1\,1\}$ planes of the fcc copper matrix in order to minimize mismatch [5,7] we get $\varepsilon \approx 0.015$. This figure is a typical value for precipitates in copper. Gerold and Pham obtained the same amount for the misfit strain of Co precipitates in Cu–Co alloys [40]. If one considers the lattice parameter $a_p = 0.368$ nm reported for a metastable chromium-rich fcc phase in quenched Cr–Ni alloy [41] as representative of fcc chromium precipitates in the present alloy, one obtains $\varepsilon \approx 0.012$. The special assumptions on the type and structure of chromium precipitates will therefore not limit the conclusions to be drawn from the calculation. The volume fractions required for the model are compiled in Table 1. With a shear modulus of $G_{1\,1\,1} = 30500$ MPa on the $\{1\,1\,1\}$ glide planes [35], [1] a Burgers vector of 2.56×10^{-10} m [42] and a value of $c_{cs} = 3$ we can derive from our data an increase of the critical resolved shear stress of 5 and 3.5 MPa for the conditions B and L, respectively. Table 4 shows that this is by far not enough to meet the experimental values. It is interesting to note that according to Gerold and Haberkorn [43] the transition from coherency strengthening to the Orowan process should take place at a critical particle radius $R_{crit.} = b/(3|\varepsilon|)$ which is 5.7 nm with the figures used here. One might argue that $\Delta\tau_0^{cs}$ depends sensitively on ε and one could reach the experimental data by assuming

[1] In fcc metals the main slip system is of the $\{1\,1\,1\}\langle 1\,\bar{1}\,0\rangle$ type. In the case of copper we have to deal with a pronounced elastic anisotropy. Therefore, the shear modulus on the glide plane, which is relevant for our quantitative comparison, $G_{\{1\,1\,1\}} = 30\,500$ MPa, differs appreciably from the isotropic value $G_{iso} = 42\,100$ MPa. Also the Poisson ratio ν, commonly assumed to be 1/3, can be calculated from the elastic constants to be 0.419 in the case of copper [35].

a much higher misfit strain of may be 0.1. This would on the other hand lead to a much lower critical radius of 0.85 nm for the transition to the Orowan mechanism.

Usually one expects the Orowan mechanism to be effective for incoherent and not shearable particles. The particles are by-passed by dislocations bowing out between two obstacles [35,36]. If we consider flexible dislocations, the spacing of the precipitates along the dislocation line in the glide plane is given by

$$L = \left(\frac{2}{f}\right)^{1/2} R, \tag{3}$$

where f and R denotes again the volume fraction of the precipitates and their mean radius, respectively [35,36]. For the Orowan mechanism the increase of the critical resolved shear stress by particle strengthening is given by

$$\Delta\tau_0 = 0.84\,\frac{2T}{bL}, \tag{4}$$

where T denotes the line tension of the dislocation line and b the modulus of its Burgers vector [36]. Since we may consider the residual concentration of solid solution atoms to be very low, the line tension values are those of pure copper. According to Mughrabi [44] the values are different for edge and screw dislocations with 1.0×10^{-9} N and 2.5×10^{-9} N, respectively. With these two figures and $b = 2.56 \times 10^{-10}$ m [42] we cover a range for the increase of the critical resolved shear stress of 58–146 and of 40–100 MPa in the conditions B and L, respectively. Table 4 compiles the relevant mechanical data as reported in [3] and the estimates of the increase of the critical resolved shear stress according to the coherency strengthening and the Orowan model. In spite of the limitations of our procedure the experimental data agree much better with the assumption of an Orowan mechanism than with the coherency strengthening model.

Strong indication of an Orowan mechanism operating in Cu–0.4 at.% Cr and Cu–Cr–Zr alloys was also reported by Long et al. [5] and Dubois and Morris [34], respectively. Long et al. [5] found good agreement between their yield stress data and the calculations on the basis of an Orowan mechanism. Their TEM investigations on deformed Cu–0.4 at.% Cr single crystals gave, however, no evidence for Orowan loops around the precipitates. It has been argued that this would not be surprising since the small Orowan loops would collapse within a fraction of a second as a result of the very high stresses acting on them due to the strong curvature of the loops. Moreover, from the absence of temperature dependence of the yield stress down to liquid nitrogen temperature, Long et al. [5] concluded that a coherency strengthening mechanism is unlikely since in this case one would expect the yield stress to decrease with lower temperature due to the decreasing misfit of the precipitates. Dubois and Morris [34] investigated the creep properties of a Cu–2Cr–0.3Zr (at.%) alloy. They found an athermal threshold stress of (95 ± 10) MPa for the dislocations to overcome the fine chromium precipitates of 25 nm in diameter observed in this alloy. This stress was identified with an calculated Orowan stress of (85 ± 15) MPa [34].

Correira et al. [9] examined the precipitation hardening in a Cu–Cr and a Cu–Cr–Zr alloy produced by water atomization and consolidated by subsequent warm extrusion. Although they used a misfit strain of $\varepsilon \approx 0.015$ in their calculations as we did, these authors found that their results are more compatible with coherency strengthening than with an Orowan model. Presumably neither the higher alloying content (> 2 at.% Cr, > 0.15 at.% Zr and > 0.2 at.% Si) nor the small grain size are the reason for this discrepancy. It is very likely caused by the presence of the bimodal precipitation distribution since a precipitate size has been used for the calculation which was obtained by TEM investigations on the consolidated material, whereas the volume fraction of the precipitates has been determined from an X-ray analysis on the powder before consolidation. In this way the overall content of chromium in solid solution was determined in the powder. From the difference with respect to the alloying content the volume fraction of chromium particles was calculated and attributed to particles with a diameter of about 4 nm. If coarse precipitates are also present in the ternary alloy of Correira et al. they missed them with such an integrating method. If so, the volume fraction of precipitates contributing to hardening would be largely overestimated by a factor 100–1000 since the largest portion of chromium is neither in solid solution nor in fine precipitates.

Although our experimental data are somehow limited and the models for precipitation hardening mechanisms deserve still further development we conclude that the Orowan mechanism describes the experimental findings in the peak hardened and slightly overaged state of our Cu–Cr–Zr alloy better than a coherency strengthening mechanism. More information on the nature of the precipitates would be required to assess possible contributions of other hardening mechanisms like modulus hardening. The latter might be important if the elastic moduli of the precipitates differ markedly from the matrix modulus.

5. Summary and conclusions

The precipitates in the investigated Cu–Cr–Zr alloy exhibit a bimodal size distribution consisting of coarse precipitates with a size of 0.2–2 μm and an interparticle distance of several μm, which we define as mesoscopic scale. The desired mechanical strength is brought about

only by tiny and finely dispersed precipitates on a microscopic scale, which exhibit strain field contrast in TEM. These precipitates have a mean size of 2.3 nm and mean three-dimensional spacings between 30 and 40 nm. The maximum observed density was 3.3×10^{22} m^{-3}. Thus, the mechanical properties are determined by less than 1% of the alloying content. Whereas the density of the tiny, microscopic precipitates depends strongly on the heat treatment of the alloy, the volume fraction of the mesoscopic, coarse particles is hardly affected by heat treatments and resists even solution annealing. The electron microscopical investigation supports the conclusions in an earlier paper of the present authors that the low cooling rates after hot isostatic pressing lead to an overaging of the alloy [3].

The identification of the nature of the microscopic precipitates failed since no additional chemical information has been available and the additional reflexes in the electron diffraction patterns could not be indexed in a consistent manner. Moreover the knowledge on the phase relations in the ternary Cu–Cr–Zr system is still insufficient. The EDX investigation of the mesoscopic precipitates is compatible with recent investigations of the phase relations indicating that the phases are Cu, pure Cr and Cu_5Zr [13,14].

The available data on precipitation hardening indicate that an Orowan mechanism can sufficiently describe the findings. A coherency strengthening mechanism can, however, not completely be ruled out since the calculations depend sensitively on the value of the misfit strain of the coherent precipitates, which might in reality be higher than that assumed for the precipitation of chromium on {1 1 1} planes of copper.

Improvements of the mechanical behaviour of the alloy depend on the success to avoid coarse precipitation during solidification or to fragment the coarse precipitates and to redistribute the alloying content. In this way the chromium and zirconium concentration in solid solution might be increased during solution annealing. Such a redistribution might be brought about by severe plastic deformation which may shear and separate the coarse precipitates. The refinement of the coarse particles may also have a positive effect on the fracture toughness since large strong particles may act as internal stress concentrators. This assumption is supported by the fact that the largest elongation at fracture was measured on tensile test specimens subjected to the heat treatment sequence G. The SEM investigation revealed in this case the smallest coarse precipitation and the most homogeneous distribution.

Probably the composition of the alloy needs further development, may be by a general slight reduction of the chromium and zirconium content and by increasing the chromium to zirconium ratio since the zirconium seems to play an essential role for coarse precipitation.

Acknowledgements

The authors are indebted to Dr F. Phillipp at the Max-Planck-Institut für Metallforschung, Stuttgart for the possibility to perform the TEM investigations there and for helpful discussions, to Mrs M. Kelsch for her technical assistance with TEM and to Dr U. Eßmann for valuable comments and critical reading of the manuscript.

References

[1] ITER Joint Central Team, J. Nucl. Mater. 212–215 (1994) 3.
[2] J.W. Davies, D.E. Driemeyer, J.R. Haines, R.T. McGrath, J. Nucl. Mater. 212–215 (1994) 1352.
[3] U. Holzwarth, M. Pisoni, R. Scholz, H. Stamm, A. Volcan, this issue, p. 19.
[4] B.N. Singh, D.J. Edwards, M. Eldrup, P. Toft, J. Nucl. Mater. 249 (1997) 1.
[5] N.J. Long, M.H. Loretto, C.H. Lloyd, Acta Metall. 28 (1980) 709.
[6] G.C. Weatherly, P. Humble, D. Borland, Acta Metall. 27 (1979) 1815.
[7] Y. Komem, J. Rezek, Metall. Trans. A 6A (1975) 549.
[8] R.W. Knights, P. Wilkes, Metall. Trans. 4 (1973) 2389.
[9] J.B. Correira, H.A. Davies, C.M. Sellars, Acta Mater. 45 (1997) 177.
[10] N.Y. Tang, D.M.R. Taplin, G.L. Dunlop, Mater. Sci. Technol. 1 (1985) 270.
[11] D.J. Chakrabati, D.E. Laughlin, Bull. Alloy Phase Diag. 5 (1984) 59.
[12] Z. Rdzawski, J. Stobrawa, Scr. Metall. 20 (1986) 341.
[13] K.J. Zeng, H. Hämäläinen, J. Alloy Compound 220 (1995) 53.
[14] K.J. Zeng, H. Hämäläinen, K. Lilius, Scr. Metall. Mater. 32 (1995) 2009.
[15] M.F. Ashby, M.L. Brown, Philos. Mag. 8 (1963) 1083.
[16] K.G. McIntyre, M.L. Brown, J. Phys. (Paris) 27 (1966) C3178.
[17] J.W. Edington, Monographs in Practical Electron Microscopy in Materials Science, Philips Technical Library, Macmillan, London, 1974.
[18] P.B. Hirsch, A. Howie, R.B. Nicholson, D.W. Pashley, M.J. Whelan, Electron Microscopy of Thin Crystals, 2nd, R.E. Krieger Publishing, Huntington, New York, 1977.
[19] H.P. Degischer, Philos. Mag. 26 (1972) 1137.
[20] P. Eckelin, H. Kandler, in: Landoldt – Börnstein Structure Data of Elements and Intermetallic Phases, vol. 6, Springer, New York, 1971.
[21] N.C. Baenziger, J. Wyart, J. Monteath Robertson (Eds.), in: A.J.C. Wilson (Ed.), Structure Reports, vol. 6, International Union of Crystallography, N.V.A. Oosthoek's Uitgevers MIJ, Utrecht, 1952, p. 5.
[22] M.V. Nevitt, J.W. Downey, Trans. Metall. Soc. AIME 224 (1962) 195.
[23] W.B. Pearson, J.M. Bijvoet, J. Donohue (Eds.), in: A.J.C. Wilson (Ed.), Structure Reports, vol. 18, International Union of Crystallography, N.V.A. Oosthoek's Uitgevers MIJ, Utrecht, 1954, p. 124.

[24] E. Kneller, Y. Khan, U. Gorres, Z. Metallkd. 77 (1986) 43.
[25] J.P. Gabathuler, P. White, E. Parthé, Acta Crystallogr. B 31 (1975) 608.
[26] S.P. Alosova, P.B. Budberg, K.I. Shakhova, Sov. Phys. – Crystallogr. 9 (1964) 343.
[27] W.B. Pearson, A Handbook of Lattice Spacings and Structures of Metals and Alloys, Pergamon, Oxford, 1967.
[28] G. Piatti, D. Boerman, J. Nucl. Mater. 185 (1991) 29.
[29] M. Apello, P. Fenici, Mater. Sci. Eng. A 102 (1988) 69.
[30] G. Falkenhagen, W. Hofmann, Z. Metallkd. 43 (1952) 69.
[31] J.P. Lynch, Wire 13 (1962) 1593,1658.
[32] S. Spaic, A. Krizman, V. Marinkovic, Metalwissen. Techn. – Met. 39 (1985) 43.
[33] M.A. Morris, M. Leboeuf, D.G. Morris, Mater. Sci. Eng. A 188 (1994) 255.
[34] C. Dubois, M.A. Morris, Scr. Metall. Mater. 30 (1994) 827.
[35] A.J. Ardell, Metall. Trans. A 16A (1985) 2131.
[36] V. Gerold, in: F.R.N. Nabarro (Ed.), Dislocations in Solids, vol. 4, North-Holland, Amsterdam, 1979, p. 219.
[37] H. Lilholt, in: J.B. Bilde-Sørensen, N. Hansen, A. Horsewell, T. Leffers, H. Lilholt (Eds.), Deformation of Multi-Phase and Particle Containing Materials, Proceedings of the Fourth Risø International Symposium on Metallurgy and Materials Science, Risø National Laboratory, Roskilde, Denmark, 1983, p. 381.
[38] U.F. Kocks, in: A.S. Argon (Ed.), Physics of Strength and Plasticity, MIT, Cambridge, MA, 1969, p. 143.
[39] J.D. Eshelby, Proc. Roy. Soc. A 241 (1957) 376.
[40] V. Gerold, H.M. Pham, Z. Metallkd. 71 (1981) 286.
[41] W.B. Pearson, A Handbook of Lattice Spacings and Structures of Metals and Alloys, Pergamon, Oxford, 1964, p. 531.
[42] P. Coulomb, Scr. Metall. 15 (1981) 769.
[43] V. Gerold, H. Haberkorn, Phys. Stat. Sol. 16 (1966) 675.
[44] H. Mughrabi, in: O. Brulin, R.K.T. Hsieh (Eds.), Continuum Models of Discrete Systems, North-Holland, Amsterdam, 1981, p. 241.